RSC Advances

ROYAL SOCIETY OF CHEMISTRY

PAPER

View Article Online
View Journal | View Issue

Cite this: *RSC Adv.*, 2024, **14**, 35671

Electromagnetic wave effects on Mn-doped superparamagnetic iron oxide nanofluids: applications in enhanced oil recovery

Mohamad Amin Bin Hamid,[ab] Beh Hoe Guan,*[ab] Chan Kar Tim[cd]
and Hassan Soleimani[ab]

Received 19th June 2024
Accepted 15th October 2024

DOI: 10.1039/d4ra04500a

rsc.li/rsc-advances

The utilization of superparamagnetic iron oxide nanofluids in enhanced oil recovery (EOR) has gained attention due to their ability to alter the interfacial tension (IFT) of reservoir rocks. However, the influence of electromagnetic (EM) waves on these nanofluids, particularly when doped with manganese (Mn), remains underexplored. The interaction mechanisms between EM waves and Mn-doped Fe_3O_4 nanofluids are not well understood, limiting their application in EOR. This study aimed to investigate the effects of EM waves on Mn-doped superparamagnetic iron oxide nanofluids and to assess the potential for enhancing oil recovery by measuring their IFT. Mn-doped Fe_3O_4 nanoparticles were synthesized using a co-precipitation method and stabilized with ascorbic acid. Density functional theory (DFT) was employed to study the Mn-dopant site selectivity within the Fe_3O_4 lattice. Helmholtz coils generated uniform EM fields and interfacial tension (IFT) measurements were conducted under applied EM waves generated under both direct current (DC) and alternating current (AC) conditions. DFT calculations indicated a preference for Mn dopants in specific lattice sites, while the experimental results showed that both DC- and AC-generated sinusoidal EM waves could reduce the IFT of the Mn-doped nanofluids, suggesting their improved EOR potential. These findings provide new insights into the application of EM waves in nanofluid-based EOR.

Introduction

The demands for energy continue to rise among globally, further increasing the need for innovative strategies to maximize hydrocarbon extraction from existing and future oil reservoirs. In this endeavor, enhanced oil recovery (EOR) offers an innovative solution to extract more oil from mature oil fields, especially by using nanotechnology.[1] Nanofluid injection can improve oil recovery by two mechanisms: by altering the wettability of the reservoir rocks to become water-wet and by reducing the interfacial tension (IFT) between oil and water phases, leading to the formation of oil droplets that are more easily mobilized.[2,3] A recent study reported a 10.8% improved oil recovery with the injection of 0.03 wt% Fe_3O_4@chitosan nanofluids into carbonate sand pack.[3]

Another underexplored mechanism in nanofluid injection EOR technique is manipulating ferromagnetic- or superparamagnetic-based nanofluids using external EM waves.[4,5] This approach leverages the inherent magnetic properties of nanoparticles such as Fe_2O_3 or Fe_3O_4, allowing remote control of their movement and distribution inside the reservoir. This mechanism allows dynamically adjusting the behavior of magnetic nanoparticles to improve the sweep efficiency by ensuring the nanoparticles are distributed to unswept areas, reducing the IFT of the oil–water phase to mobilize trapped oil droplets, and altering the wettability of reservoir rock to improve oil displacement. Yarima *et al.* (2022)[4] observed a decrease in the IFT when Fe_2O_3, SiO_2, ZnO, and brine were exposed to EM waves. They highlighted that the ability of materials to polarize and absorb the energy from propagating EM waves plays a crucial role in the reduction of the IFT. Enhancing the magnetic properties of materials such as Fe_3O_4 can improve their application in EM-waves-assisted EOR. One key approach to achieve this is through substitutional doping with transition metals, such as manganese (Mn), zinc (Zn), and cobalt (Co), into the crystal structure of Fe_3O_4.[6–10] Previous studies found that substitutionally doping Co into Fe_3O_4 could increase the magnetic saturation and coercivity, making it suitable for applications with hard magnets or magnetic hyperthermia.[11,12]

---

[a] Department of Fundamental & Applied Sciences, Universiti Teknologi Petronas, Seri Iskandar 32610, Perak, Malaysia. E-mail: beh.hoeguan@utp.edu.my; Fax: +60 108946521; Tel: +60 108946521

[b] Centre of Innovative Nanostructure and Nanodevices, Universiti Teknologi Petronas, Seri Iskandar 32610, Perak, Malaysia

[c] Department of Physics, Faculty of Science, University Putra Malaysia, Serdang, Malaysia

[d] Laboratory of Computational Sciences and Mathematical Physics, Institute for Mathematical Research, Universiti Putra Malaysia, Malaysia

However, magnetic nanoparticles, such as Fe_3O_4, tend to agglomerate and clump together once the EM waves are removed. This is also due to the high surface area to volume ratio needed to produce superparamagnetism in Fe_3O_4, which leads to large van der Waal interactions. Often, surfactants, such as sodium dodecyl sulfate (SDS), are needed to coat the outer surface of the nanoparticles to overcome the large van der Waal interaction between Fe_3O_4 nanoparticles.[13–15] Nonetheless, the idea of pumping heavy chemical surfactants raises some concerns related to underground pollution. An alternative is to use organic acids, such as ascorbic acid or citric acid, which are more environmentally friendly.[16,17] Our previous work found that ascorbic acid-coated zinc ferrite nanofluid formed a stable dispersion with good wettability alteration properties at a 0.25 M ascorbic acid concentration.[16] In the present study, we aimed to investigate the effects of EM waves on Mn-doped Fe_3O_4 nanofluids and to assess their potential for EOR applications. In this study, we synthesized Mn-doped Fe_3O_4 nanoparticles and stabilized them by coating them with ascorbic acid. Then, we created Mn-doped Fe_3O_4 nanofluids by using 30 000 ppm as the base fluid and measured the IFT under the influence of direct current (DC) and alternating current (AC) EM waves.

Methodology

To better understand the effects of Mn doping on Fe_3O_4, we also employed first-principle calculations using density functional theory (DFT). The structure of Fe_3O_4 is depicted in Fig. 1. The DFT package (Quantum ESPRESSO) used the general gradient approximation (GGA) pseudopotential and Perdew–Burke–Ernzerhof for Solid (PBEsol) exchange–correlation function, which is a revised version of PBE.[18,19] The preliminary density functional theory (DFT) calculation was done using the Hubbard + U correction to consider the strong electron correlation in 3d metals such as Fe and Mn.[20] In DFT+U computations, an additional value is added to correct the approximate DFT energy functional to describe the on-site coulombic repulsion between the electrons in d-orbitals.

$$E_{\mathrm{DFT}+U} = E_{\mathrm{DFT}} + E_U$$

In the crystal structure of Fe_3O_4, the electrons in the valence 3d orbitals strongly interact with each other, which cannot be accurately described using standard DFT. The correction $U = 3$ eV was chosen here for the Fe atoms while $U = 1$ eV was used for the Mn dopants. For the oxygen (O) ions, the Hubbard parameter was maintained at 0 eV.

The co-precipitation methodology utilized in this study was based on our previous report on ascorbic acid-coated Fe_3O_4.[16] $Mn_xFe_{2-x}O_4$ ($x = 0$, 0.25, 0.5 and 0.75) was thus synthesized by co-precipitation. Here, iron(II) chloride, iron(III) chloride, and manganese nitrate salts were mixed together into a solution of distilled water at different stoichiometric ratios depending on the concentration x. Then, 3 M potassium hydroxide was added into the mixture to make it alkaline (up to pH 12). A black precipitate was then formed from the reaction. The mixture was then constantly stirred at 500 rpm for 20 min to ensure that the reaction was complete. The black precipitate was repeatedly filtered, dried, and washed at least 3 times to remove excess supernatant and then air dried at 60 °C for 12 h. Once dried, the black precipitate was ground into a fine powder. The coating of ascorbic acid was done by immersing the black powder of $Mn_xFe_{2-x}O_4$ into a beaker of y M ($y = 0.1$, 0.2, 0.3, 0.4, and 0.5) ascorbic acid for 20 min before filtering using a magnet, and then washed and dried. Next, 0.01 and 0.05 wt% $Mn_xFe_{2-x}O_4$ nanofluids were obtained by immersing the powder into NaCl brine solutions at 30 000 ppm, and ultrasonicated was continued for 10 min to ensure dispersion of the ascorbic acid-coated $Mn_xFe_{2-x}O_4$ inside the nanofluid.

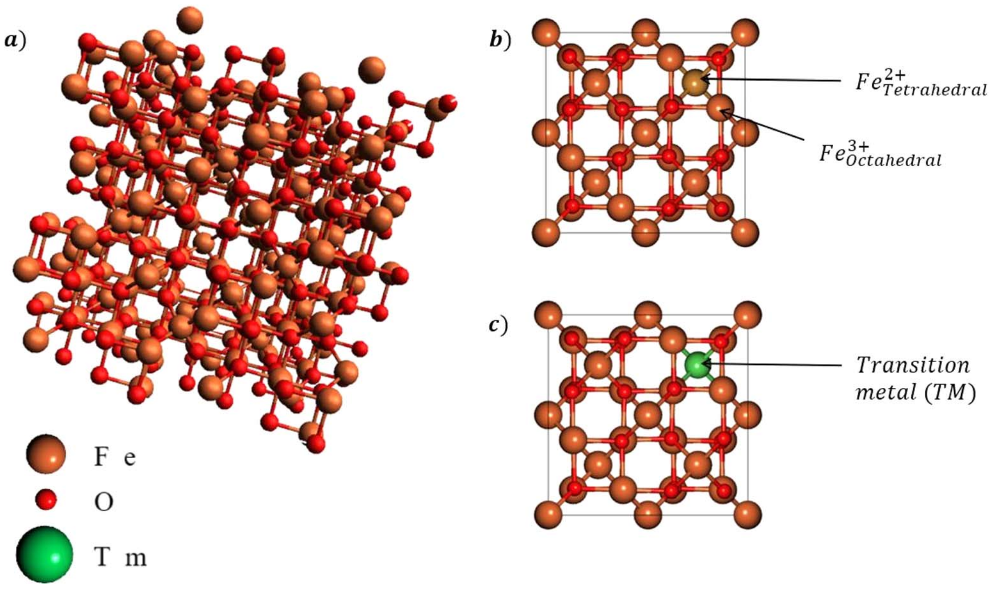

Fig. 1 (a) Cubic lattice structure of Fe_3O_4 and the (b) octahedral and tetrahedral sites. Mn dopants will be substituted into either site as shown in (c).

The formation of $Mn_xFe_{2-x}O_4$ was confirmed using X-ray diffraction (XRD). Once confirmed, field emission electron microscopy and vibrating sample magnetometry (VSM) were performed to study the surface morphology and magnetic properties of $Mn_xFe_{2-x}O_4$. Then, pendant drop measurements were performed to investigate the interfacial tension of the ascorbic acid-coated $Mn_xFe_{2-x}O_4$ nanofluid. Due to the magnetic nature of our nanofluid, we extended the studies to also include testing the effects of the magnetic field. The experimental setup is illustrated in Fig. 2, where a Helmholtz coil was used to produce a uniform field in between two sets of coils of copper wire. XRD analyses was carried out using a Panalytical Xpert3 Powder X-ray diffractometer at 300 K. FESEM was carried out using a Zeiss-Supra 55VP electron microscope, while the hysteresis loop was measured using a 7400 Series VSM system.

Results and discussion

The Mn doping site selectivity was explored between the tetrahedral and octahedral sites for Mn substitution, whereby the Mn dopants replaced either Fe^{3+} at the tetrahedral sites or Fe^{2+} at the octahedral sites. This was done by comparing the doping effects on the formation energy, total magnetic moment, and lattice constant, as presented in Table 1. From Table 1, it can be seen that the tetrahedral substitution was slightly preferred, even though the differences in the formation energy were relatively small, indicating mixed substitution. This helped elucidate the co-precipitation of $Mn_xFe_{2-x}O_4$ ($x = 0$, 0.25, 0.5, and 0.75). The lattice constant between the two sites showed a contraction in comparison with Fe_3O_4 (8.505 Å). Fig. 3 presents the simulated XRD patterns of $Mn_xFe_{2-x}O_4$, indicating a slight shift of the XRD spectra to lower angles, likely due to the increasing volume per unit cell of $Mn_xFe_{2-x}O_4$.

Table 1 Lattice constant, formation energy, and total magnetic moment of $Mn_xFe_{3-x}O_4$

	Lattice constant (Å)	Formation energy (eV)	Total magnetic moment (μ_{Bohr})
Tetrahedral	8.423	−0.382	4.374
Octahedral	8.352	−0.379	0.3

A critical aspect of the XRD analysis in Fig. 3 is the observation of peak modifications, particularly the formation of doublets and shifts in the peak positions. In the case of tetrahedral doping with Zn and Mn, there was no formation of doublets in the XRD patterns. The absence of doublets in tetrahedral doping indicated that the substitution of Fe ions by the dopants did not significantly distort the lattice to an extent that would cause splitting of the diffraction peaks. This suggests that the dopants were incorporated into the lattice in a manner that preserves the overall symmetry and structure of the Fe_3O_4 crystal. In contrast, the XRD patterns for octahedral

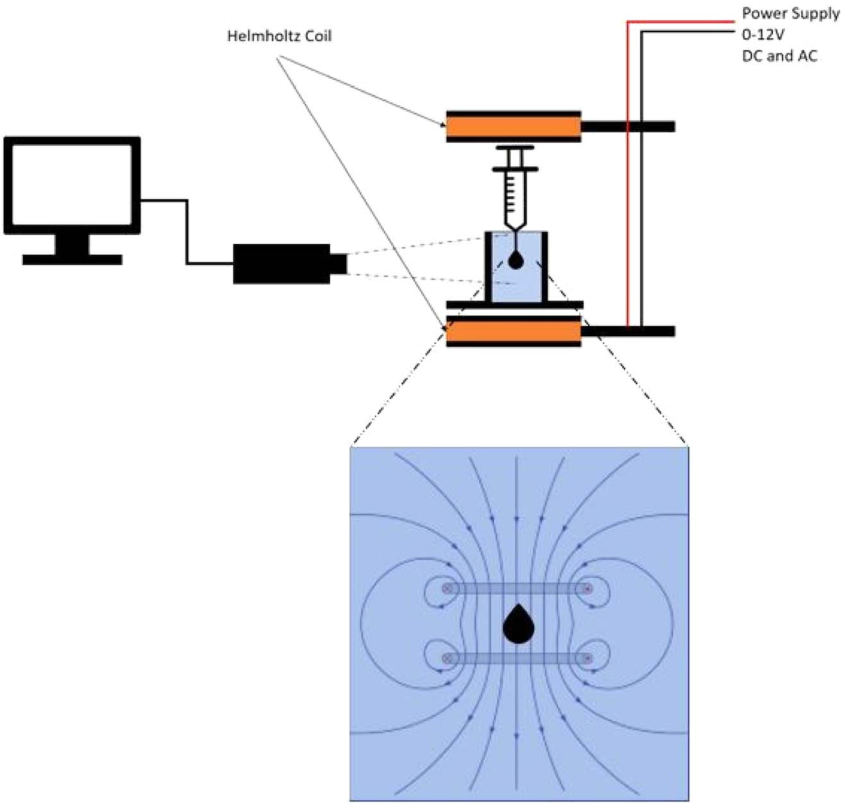

Fig. 2 Setup for the interfacial tension (IFT) measurements under the influence of direct current (DC) and alternating current (AC) used to generate electromagnetic field through a Helmholtz coil.

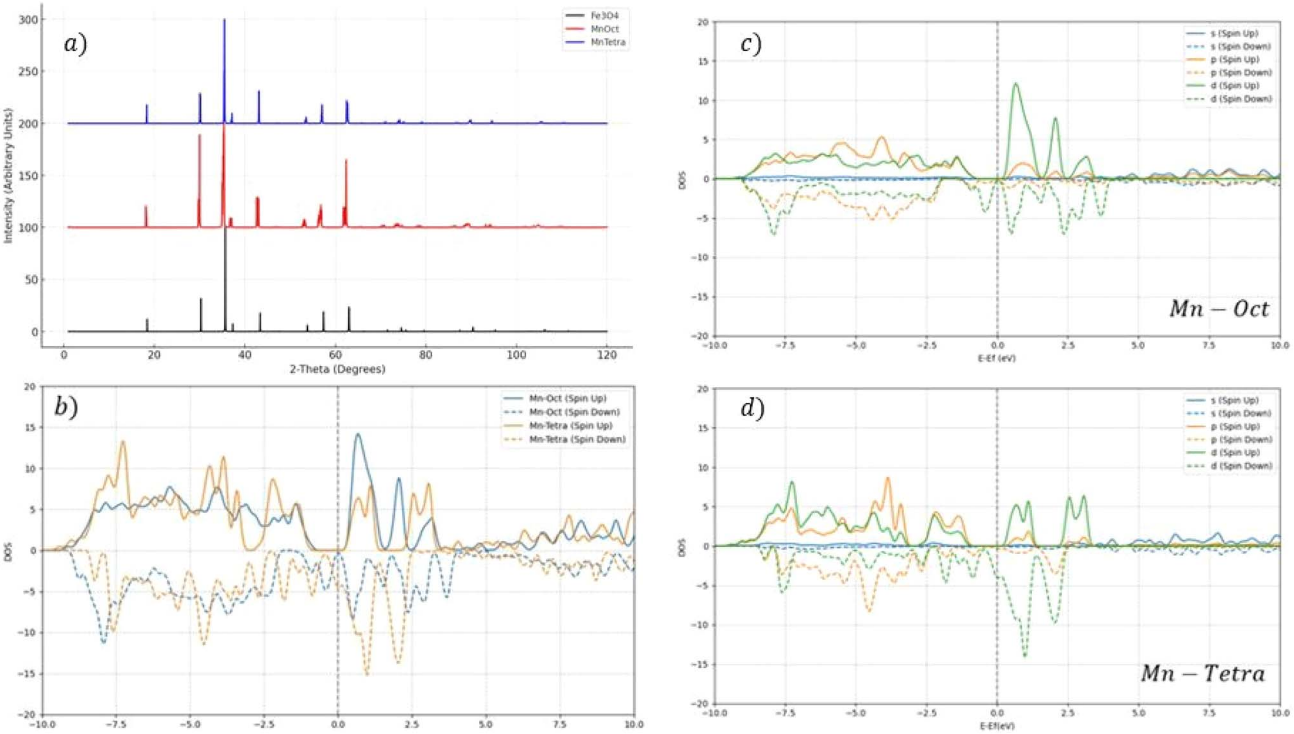

Fig. 3 (a) Simulated XRD pattern obtained by VESTA analysis of $Mn_xFe_{2-x}O_4$, where one Mn atom replaces one Fe atom at either a tetrahedral or octahedral site. (b) Total density of states, (c and d) partial density of states of tetrahedral and octahedral Mn-substituted Fe_3O_4.

doping exhibited a slight broadening, indicating the formation of doublets. The appearance of doublets in these patterns was indicative of a more pronounced lattice distortion caused by the substitution of Fe ions at the octahedral sites.

From Table 1, it can be seen that the tetrahedral substitution led to an increase in the total magnetic moment compared to Fe_3O_4 ($3.9\mu_{\text{Bohr}}$), while octahedral substitution led to a decrease in the total magnetic moment. The substitution of a transition metal, such as Mn, at either tetrahedral or octahedral sites can lead to increasing or reducing the total magnetic moment due to the disruption of either mechanism. In the superexchange mechanism, the magnetic moments of Fe^{3+} ions are coupled through an oxygen ion, leading to a characteristic antiferromagnetic alignment, while the double exchange mechanism is a direct interaction that primarily occurs between Fe^{2+} and Fe^{3+} ions at the octahedral sites of the Fe_3O_4 lattice facilitated by the overlapping of the d-orbitals of adjacent Fe ions, allowing for the transfer of electrons between Fe^{2+} and Fe^{3+} states. Half-metallicity is a unique electronic property characterized by a material exhibiting metallic behavior for electrons of one spin channel, while maintaining a semiconducting or insulating behavior for electrons of the opposite spin channel. This phenomenon can be clearly observed in the density of states (DOS) plot in Fig. 3b, where the spin-up channel DOS has zero population, indicating a gap near the Fermi level, while the spin-down channel has a significant population.

The s-orbital contribution was relatively small across the energy spectrum, which is typical as s orbitals are often fully occupied first. The p- and d-orbital contributions showed more significant DOS, with peaks both below and above the Fermi level, indicating that p orbitals contributed to both bonding/valence band states and unoccupied/conduction band states. For both the p- and d-orbitals, there were noticeable differences between the spin-up and spin-down channels, indicating magnetic behavior or spin polarization in the material. The presence of overlapping peaks in the p- and d-orbital contributions to the DOS near the Fermi level suggested hybridization between these orbitals, which commonly occurs between a metal's d-orbitals and the p-orbitals of the surrounding ligands.

The characteristics peaks of Fe_3O_4 are shown and labeled (220), (311), (400), (422), and (511) in Fig. 4. The peaks were found in all the samples, indicating the characteristics of an inverse spinel structure was maintained even when doped by Mn ions. A subtle shift to lower angles was found in all the doped samples, suggesting an expansion of the unit cell volume, which might be due to the differences in ionic radii of Mn^{2+} ions compared to Fe^{2+}/Fe^{3+} ions. Further study of the FESEM micrograph in Fig. 4 revealed a clear trend of increasing average particle size and agglomeration, where nanoparticles were clustered together, as the Mn doping concentration increased. All the $Mn_xFe_{2-x}O_4$ ($x = 0.25$, 0.5, and 0.75) nanoparticles displayed a superparamagnetic behavior (coercivity → 0). Increasing the Mn-dopant concentrations showed a decreasing magnetic saturation (M_s). This was due to the substitution of ferromagnetic Fe^{2+}/Fe^{3+} ions with diamagnetic Mn^{2+} ions, which interferes with the electron-exchange mechanism (double- and superexchange mechanism) in the inverse

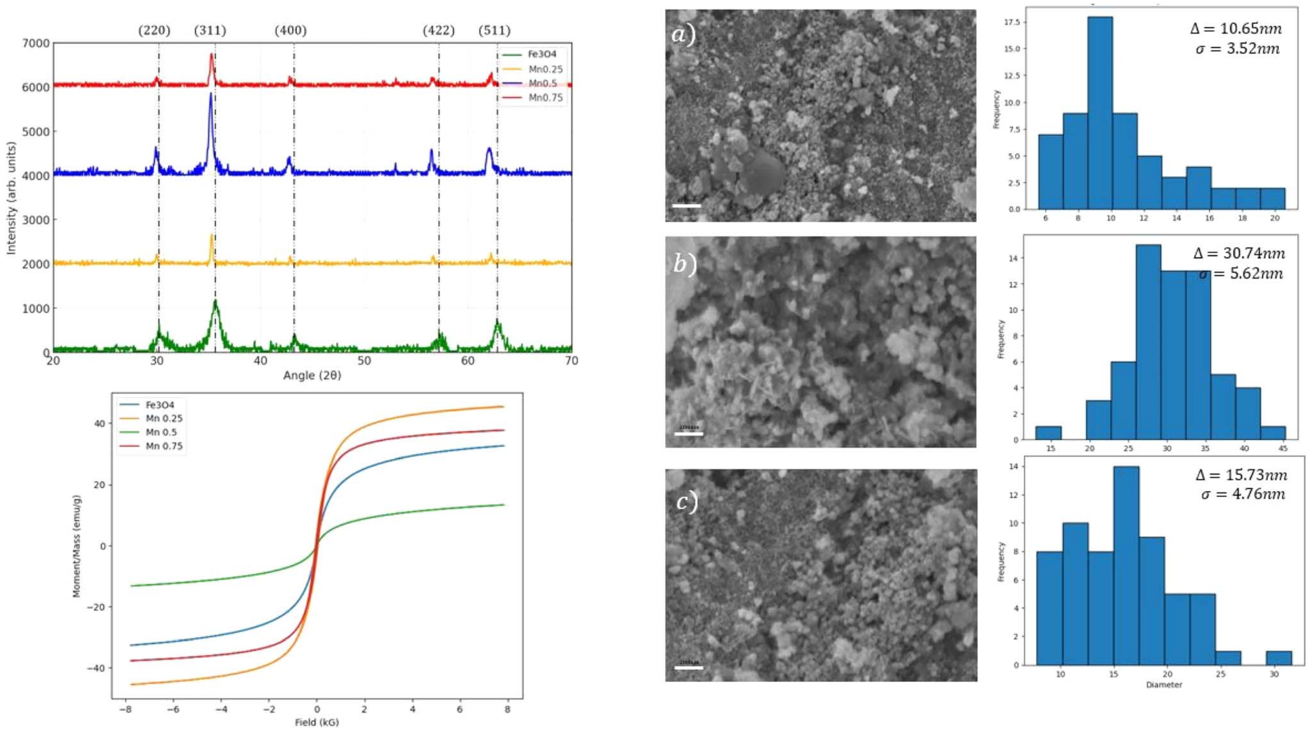

Fig. 4 XRD spectra, hysteresis loops, and FESEM micrographs of (a–c) $Mn_xFe_{2-x}O_4$ ($x = 0.25$, 0.5 and 0.75). The histogram illustrates the distribution of the average nanoparticle size.

spinel structure of Fe_3O_4, leading to a reduction in the net magnetic moment and Ms. However, the lowest Ms recorded was when the Mn-doping concentration was at $x = 0.5$ with Ms less than 10 emu g^{-1}. Thorough observation by the FESEM micrograph showed that there was some formation of rod-like structures other than the almost spherical structure of $Mn_xFe_{2-x}O_4$. This might have contributed to the lowering of the Ms of $Mn_xFe_{2-x}O_4$ at Mn = 0.5, along with the increase in the average nanoparticle size to around 30 nm. The sharper XRD peaks also suggested a higher crystallinity of Mn = 0.5 doped Fe_3O_4 compared to the others. Generally, the shape anisotropy plays an important role in determining the magnetic properties of Fe_3O_4, with a certain shape and morphology exhibiting a higher magnetic saturation compared to others.[21]

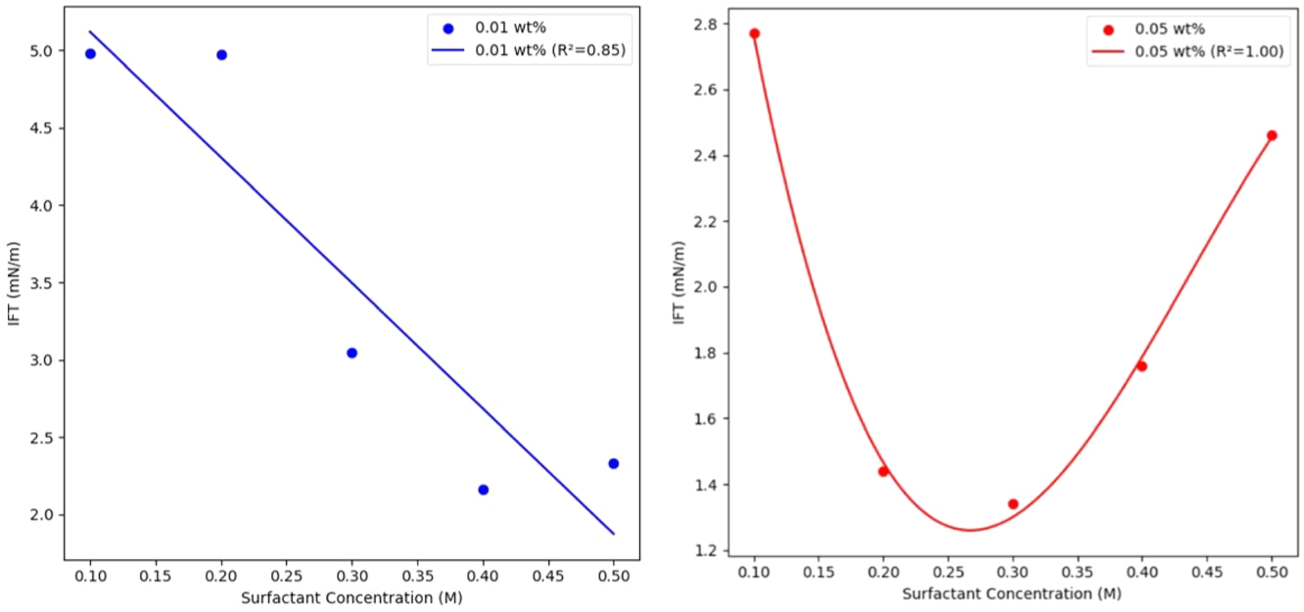

Fig. 5 Interfacial tension (IFT) of ascorbic acid-coated $Mn_{0.75}Fe_{2.25}O_4$/NaCl brine nanofluid *vs.* the ascorbic acid concentration at 0.01 and 0.05 wt% nanofluid concentrations.

Fig. 5 shows the interfacial tension (IFT) of ascorbic acid-coated $Mn_{0.75}Fe_{2.25}O_4$/NaCl brine nanofluid under the effects of the different ascorbic acid concentrations used (0.01 and 0.05 wt%). Generally, the IFT showed a distinct behavior for the 0.01 and 0.05 wt% nanofluid concentration trendlines. For the 0.01 wt% nanofluid, the IFT displayed a decreasing trend as the surfactant concentration increased, showing a strong linear dependency (*R*-squared = 0.85). In contrast, the 0.05 wt% nanofluid also showed a decreasing trend in the IFT with increasing the surfactant concentration, but this relationship showed a strong quadratic dependency (*R*-squared = 1). This perfect fit suggested a very strong non-linear relationship between the IFT and surfactant concentration, indicating that at much higher nanofluid concentrations, the relationship between the IFT and surfactant concentration was more complex and could only be explained in a non-linear manner. Similar trends were also reported by Paryoto *et al.* (2023),[22] where a non-linear behavior in the IFT was reported with increasing the concentration of a surfactant with either an anionic or amphoteric nature. They reported that at lower concentrations, the surfactant was effectively adsorbed at the oil–water interface, leading to a significant reduction in IFT, but as the concentration of the surfactant increased, the interface reached saturation, whereby the excess surfactant began forming micelles in the bulk solution instead. However, the study did not explicitly state that the IFT increased when the surfactant concentration increased beyond a critical point. Molecular dynamics simulation of three sodium branched-alkylbenzene sulfonates at the nonane–water interface were done by Liu *et al.* (2017)[23] and supported the observation of critical surfactants concentrations, where the ability to further reduce the IFT was reduced.

Considering the magnetic nature of the ascorbic acid-coated $Mn_{0.75}Fe_{2.25}O_4$/NaCl brine nanofluid, we next studied the effects of the electromagnetic field (EM) on the IFT. The electromagnetic field was generated using a Helmholtz coil, from which direct current (DC) and alternating current (AC) were supplied. The DC supply produced a constant magnetic field while the AC supply produced a fluctuating magnetic field (sinusoidal). Fig. 6 illustrates the effects of the applied EM field on the IFT of the 0.01 wt% ascorbic acid-coated $Mn_{0.75}Fe_{2.25}O_4$/NaCl brine nanofluid. Linear regression was applied to both the AC (blue line) and DC (yellow line) trends. Generally, the IFT of the ascorbic acid-coated $Mn_{0.75}Fe_{2.25}O_4$/NaCl brine nanofluids showed a decreasing trend for both the AC and DC trendlines. With increasing the voltage supplied (9–12 V), the trendline for both AC and DC seemed to be flatter, indicating that the effect of the surfactant concentration on the IFT became less significant at a much higher voltage. The EM waves generated by AC voltage reduced the IFT of the ascorbic acid-coated $Mn_{0.75}Fe_{2.25}O_4$/NaCl brine nanofluid more, with a steeper decrease compared to the DC voltage, indicating that fluctuating EM waves were much more effective in reducing the IFT. However, the R^2 of the AC series was much weaker than with the

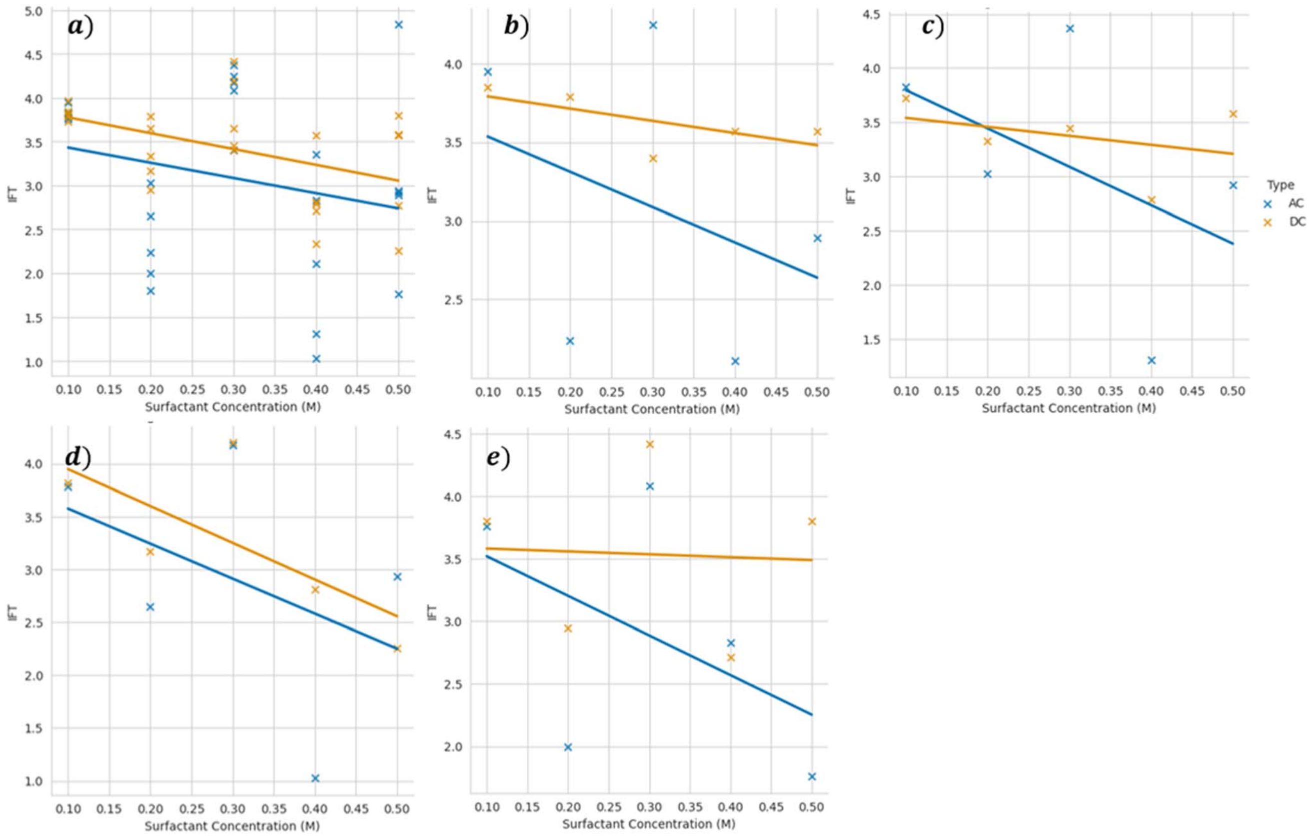

Fig. 6 Interfacial tension of 0.01 wt% ascorbic acid-coated $Mn_{0.75}Fe_{2.25}O_4$/NaCl brine nanofluid *vs.* the ascorbic acid concentration at varying voltages of (a) 2, (b) 4, (c) 6, (d) 9, and (e) 12 V.

DC voltage, indicating a possible non-linear relationship between the EM applied and IFT, which could be further explored. Comparing Fig. 5 and 6, it could be observed that the application of EM waves reduced the IFT. In between 2–12 V, the IFT was reduced by 1.01 mN m^{-1} (2 V) to 1.18 mN m^{-1} (12 V) for the 0.1 M ascorbic acid concentration when DC EM waves were applied. When AC EM waves were applied, the IFT was reduced further by 1.16 mN m^{-1} (2 V) to 1.22 mN m^{-1} (12 V). A similar trend in the reduction of IFT was found across the different ascorbic acid concentrations, with AC EM waves contributing to a higher reduction compared to DC EM waves. Due to the fluctuating nature of the AC current, the EM waves produced also fluctuate, causing the affected nanoparticles to be unable to quickly polarize with the changing polarity inside the nanofluids. DC EM waves have constant polarity, which allows the nanoparticles inside the nanofluid to polarize and agglomerate.

Conclusions

In conclusion, this study provides valuable insights into the effects of doping on Fe_3O_4 at low concentrations of Mn dopants. Our findings found that there were small preferences for tetrahedral sites, although the differences in formation energy were very small, indicating a mixed distribution of dopants across both tetrahedral and octahedral sites. Mn dopants were found to improve the total magnetic moment per unit cell of Fe_3O_4 when doped at tetrahedral sites, due to the disruption of the superexchange mechanism. The density of states study also revealed the half-metallicity properties of $Mn_xFe_{2-x}O_4$ when doped at both octahedral and tetrahedral sites The co-precipitation of $Mn_xFe_{2-x}O_4$ (x = 0.25, 0.5, and 0.75) was successfully performed. The magnetic characterization through VSM verified the superparamagnetic properties, with $Mn_{0.25}Fe_{2.75}O_4$ having the lowest average nanoparticle size and highest magnetic saturation, showing the size dependency of the magnetic properties of the nanoparticles. The interfacial tension of the 0.01 wt% ascorbic acid-coated $Mn_{0.25}Fe_{2.75}O_4$/NaCl nanofluid was found to have an inverse and strong linear relationship (R-squared = 0.85) with the ascorbic acid concentration and applied electromagnetic field. In contrast, the 0.05 wt% nanofluid showed a quadratic relationship between the IFT of the nanofluid and the ascorbic acid concentration, showing a strong non-linear relationship (R-squared = 1). Although having a weak linear relationship, the electromagnetic waves produced by AC power supply were found to lead to a much steeper decrease in interfacial tension when compared to DC power supply.

Data availability

All the data generated or analysed during this study are included in this published article.

Conflicts of interest

There are no conflicts to declare.

Acknowledgements

The authors express their appreciation to Yayasan Universiti Teknologi PETRONAS for the financial support for this study in the form of a research grant (YUTP Cost Centre: 015LC0-334). During the preparation of this work the authors used Quillbot to paraphrase and edit the documents. After using this tool/service, the authors reviewed and edited the content as needed and takes full responsibility for the content of the publication.

References

1 A. H. Abbas, W. R. W. Sulaiman, M. Z. Jaafar, A. O. Gbadamosi, S. S. Ebrahimi and A. Elrufai, Numerical study for continuous surfactant flooding considering adsorption in heterogeneous reservoir, *J. King Saud Univ., Eng. Sci.*, 2020, **32**(1), 91–99.
2 J. A. Ali, K. Kolo, A. K. Manshad and K. D. Stephen, Potential application of low-salinity polymeric nanofluid in carbonate oil reservoirs: IFT reduction, wettability alteration, rheology and emulsification characteristics, *J. Mol. Liq.*, 2019, **284**, 735–747.
3 S. Paryoto, Y. Romdoni, I. Kurnia, O. Muraza and M. Khalil, Synergy of surfactant mixtures and Fe_3O_4 nanoparticles for Enhanced oil recovery (EOR), *Inorg. Chem. Commun.*, 2023, **155**, 111125.
4 Y. M. Hassan, B. H. Guan, L. K. Chuan, S. Sikiru, A. A. Adam and B. A. Abdulkadir, Interfacial tension of brine-oil interface using Fe_2O_3, ZnO, and SiO2 nanoparticles endorsed by electromagnetic waves, *Chem. Thermodyn. Therm. Anal.*, 2022, **8**, 100083.
5 Y. M. Hassan, *et al.*, Electromagnetically Modified Wettability and Interfacial Tension of Hybrid ZnO/SiO2 Nanofluids, *Crystals*, 2022, **12**(2), 169.
6 P. Saha, R. Rakshit and K. Mandal, Enhanced magnetic properties of Zn doped Fe3O4 nano hollow spheres for better bio-medical applications, *J. Magn. Magn. Mater.*, 2019, **475**, 130–136.
7 F. S. Sheik, M. A. Dar, N. Mythili and G. V. Prasath, Ferromagnetism behavior of Ni-doped Fe3O4 thin films synthesized by the SILAR technique, *Inorg. Chem. Commun.*, 2024, **165**, 112485.
8 J. Halder, P. De, D. Mandal and A. Chandra, Bricks of Co, Ni doped Fe3O4 as high performing pseudocapacitor electrode, *J. Energy Storage*, 2023, **58**, 106391.
9 Z. Chen, *et al.*, Magnetic Mn-Doped Fe3O4 hollow Microsphere/RGO heterogeneous Photo-Fenton Catalyst for high efficiency degradation of organic pollutant at neutral pH, *Mater. Chem. Phys.*, 2019, **238**, 121893.
10 P. Esmaeilnejad-Ahranjani, M. Lotfi, A. Zahmatkesh and A. A. Esskandary, Cu-doped Fe3O4 nanoparticles for efficient detoxification of epsilon toxin: Toward substituting magnetically recyclable detoxifying agent for formaldehyde, *Toxicon*, 2024, **242**, 107707.
11 R. Das, N. P. Kim, S. B. Attanayake, M. H. Phan and H. Srikanth, Role of Magnetic Anisotropy on the

Hyperthermia Efficiency in Spherical $Fe_{3-x}Co_xO_4$ (x = 0–1) Nanoparticles, *Appl. Sci.*, 2021, **11**(3), 930.

12 Z. E. Gahrouei, S. Labbaf and A. Kermanpur, Cobalt doped magnetite nanoparticles: Synthesis, characterization, optimization and suitability evaluations for magnetic hyperthermia applications, *Phys. E*, 2020, **116**, 113759.

13 S. Paryoto, Y. Romdoni, I. Kurnia, M. Marteighianti, O. Muraza and M. Khalil, Spontaneous imbibition of amphoteric-anionic surfactant and Fe3O4 nanoparticles colloidal mixture for enhanced oil recovery, *J. Mol. Liq.*, 2023, **392**, 123458.

14 J. Lei, Z. Luo, S. Qing, X. Huang and F. Li, Effect of surfactants on the stability, rheological properties, and thermal conductivity of Fe3O4 nanofluids, *Powder Technol.*, 2022, **399**, 117197.

15 S. Paryoto, Y. Romdoni, I. Kurnia, O. Muraza and M. Khalil, Synergy of surfactant mixtures and Fe3O4 nanoparticles for Enhanced oil recovery (EOR), *Inorg. Chem. Commun.*, 2023, **155**, 111125.

16 H. B. Guan, D. M. Hakim, K. Hastuti and A. M. Bin Hamid, Nano-surface Functionality of Zinc Ferrite: Ascorbic Acid Nanofluid Application in Enhanced Oil Recovery, *Nanosci. Nanotechnol.–Asia*, 2022, **12**(4), 46–52.

17 M. A. Dheyab, A. A. Aziz, M. S. Jameel, O. A. Noqta, P. M. Khaniabadi and B. Mehrdel, Simple rapid stabilization method through citric acid modification for magnetite nanoparticles, *Sci. Rep.*, 2020, **10**(1), 10793.

18 P. Giannozzi, *et al.*, QUANTUM ESPRESSO: a modular and open-source software project for quantum simulations of materials, *J. Phys.: Condens.Matter*, 2009, **21**(39), 395502.

19 J. P. Perdew, *et al.*, Restoring the Density-Gradient Expansion for Exchange in Solids and Surfaces, *Phys. Rev. Lett.*, 2008, **100**(13), 136406.

20 N. Naveas, R. Pulido, C. Marini, J. Hernández-Montelongo and M. M. Silván, First-principles calculations of hematite (α-Fe2O3) by self-consistent DFT+U+V, *iScience*, 2023, **26**(2), 106033.

21 M. M. Ba-Abbad, A. Benamour, D. Ewis, A. W. Mohammad and E. Mahmoudi, Synthesis of Fe3O4 Nanoparticles with Different Shapes Through a Co-Precipitation Method and Their Application, *JOM*, 2022, **74**(9), 3531–3539.

22 S. Paryoto, Y. Romdoni, I. Kurnia, O. Muraza and M. Khalil, Synergy of surfactant mixtures and Fe3O4 nanoparticles for Enhanced oil recovery (EOR), *Inorg. Chem. Commun.*, 2023, **155**, 111125.

23 Z. Y. Liu, *et al.*, Characterizing the impact of surfactant structure on interfacial tension: a molecular dynamics study, *J. Mol. Model.*, 2017, **23**(4), 112.